Moriche, M., Gonzalo, A., Flores, O., García-Villalba, M. (2021). Three-dimensional effects on plunging airfoils at low Reynolds numbers. *AIAA Journal*, 59(1), 65-74.

DOI: https://doi.org/10.2514/1.J058569

# Three-dimensional effects on plunging airfoils at low Reynolds numbers *

M. Moriche†
*Inst. for Hydromechanics, Karlsruhe Institute of Technology, Karlsruhe 76131, Germany*

A. Gonzalo‡
*Mechanical and Aerospace Eng. Dept., University of California San Diego, San Diego, CA 92161*

O. Flores§, M. García-Villalba¶
*Bioengineering and Aerospace Eng. Dept., Carlos III University of Madrid, Leganés 28911, Spain*

**We present 2D and 3D direct numerical simulations of large amplitude plunging maneuvers at Reynolds numbers $Re = 1000$ and $5000$, with velocity ratios $G = 0.5$, $1$ and $2$. For all cases, the evolution of the force coefficients is qualitatively similar. The lift coefficient presents a pronounced peak towards the end of the acceleration phase of the maneuver, a local minimum in the deceleration phase and a second peak at the end of the maneuver. The amplitude of the main peak increases linearly with $G$, with limited effect of $Re$ and a negligible effect of the three-dimensionality of the flow. On the other hand, both $Re$ and three-dimensionality have a stronger effect on the amplitude of the maximum value of the lift coefficient at the end of the maneuver, and on the subsequent transient decay towards the static values. The comparison of the evolution of the flow structures near the airfoil shows that these differences in the force coefficients are due to subtle interactions between the various vortices generated during the maneuver, and to the development of a 3D boundary layer on the suction side of the airfoil triggered by the instability of the trailing edge vortices.**

## Nomenclature

$\alpha$ = angle of attack

$c$ = wing chord

$c_d$ = drag coefficient

$c_l$ = lift coefficient

$c_l^{\text{static}}$ = static value of the lift coefficient at a fixed $\alpha$

*AIAA paper 2019-0640. AIAA SciTech, San Diego, California, 2019
†Postdoctoral researcher
‡Postdoctoral researcher
§Associate Professor
¶Associate Professor, Senior Member AIAA

$c_l^{peak}$ = peak lift coefficient

$\Delta c_l$ = lift coefficient increment with respect to the static value

$\Delta x$ = grid spacing

$F_x$ = aerodynamic force per unit span in the streamwise direction

$F_z$ = aerodynamic force per unit span in the vertical direction

$G$ = velocity ratio, $V/U_\infty$

$h(t)$ = vertical displacement of the airfoil

$\dot{h}$ = plunge velocity

$L_y$ = length of the computational domain along the spanwise direction

$\omega_y$ = spanwise component of the vorticity

$Q$ = 2nd invariant of the velocity gradient tensor

$Re$ = Reynolds number, $U_\infty c/\nu$

$T$ = duration of the maneuver

$t$ = time

$t_0$ = starting time

$U_\infty$ = free stream velocity

$u_x$ = streamwise component of the velocity

$u_y$ = spanwise component of the velocity

$u_z$ = vertical component of the velocity

$V$ = maximum vertical velocity of the airfoil

$\nu$ = kinematic viscosity

$x$ = streamwise direction

$y$ = spanwise direction

$z$ = vertical direction

$\overline{(.)}$ = spanwise-average of a quantity

$(.)^{std}$ = spanwise standard-deviation of a quantity

# I. Introduction

During the last decade there has been a growing interest in the development of Micro Air Vehicles (MAVs). The typical size and flight velocity of MAVs result in relatively low Reynolds numbers. As a consequence, the aerodynamics of MAVs is very different from that of conventional aircraft, being characterized by thick boundary layers, massive separation of the flow, etc. In addition, the flight dynamics of MAVs may be significantly influenced by their flight

environment. For a conventional aircraft (i.e., characteristic chord of 1m, characteristic velocity of about 100m/s) at flight levels of 10.000 − 20.000ft, the characteristic length of a gust is 20 m and a representative peak gust velocity is 5 m/s [1]. Hence, the gust is a small velocity perturbation affecting the wing as a whole, and its effect can be easily linearized [2]. On the other hand, the characteristic lengths and velocities of MAVs (i.e., 0.1m and 1m/s, respectively [3]) are of the same order of magnitude as the velocity perturbations of the air turbulence. Therefore, the response of MAVs to gusts is a fully-nonlinear problem that needs to be addressed either by experiments or simulations of specific configurations, hindering the process of obtaining a general understanding of the problem.

Due to the random nature of the velocity fluctuations in the atmosphere, the definition of a *typical* gust is challenging. There are several models of gusts studied in the literature, depending on their time history (periodic or transient), the direction of the velocity perturbation (transverse or longitudinal gusts) and their spatial distribution (localized velocity perturbations, or plunge/surge motion of the airfoil). Many of these models of gusts have been studied in the literature. For instance, authors have reported numerical and experimental results for periodic longitudinal gusts [4, 5], transient localized transverse gusts [6], transient plunge maneuvers [7–9] and for vortical gusts [10, 11], where the gust is induced by a passing vortex over the airfoil. The latter differs with respect to the others in that the gust intensity (i.e. the vortex circulation) varies due to the interaction with the airfoil. Overall, the comparison between all these gusts models is difficult, and indeed the definition of a set of *standard* large-amplitude gusts has been one of the objectives of the STO Group AVT-282, *Unsteady aerodynamic response of rigid wings in gust encounters*.

For their relevance for the present study, we review briefly some works on transient transverse gusts. Perrotta and Jones [6] performed experiments on a flat-plate that was towed through a vertical jet (i.e., a localized transverse gust). The peak velocity was of the same order of magnitude as the towing velocity (gust ratios $G = V/U_\infty = 0.42 - 1.68$, where $U_\infty$ is the towing velocity and $V$ is the maximum vertical velocity of the jet), and the Reynolds number ranged between $Re = 10000$ and 40000, based on $U_\infty$ and the chord of the airfoil, $c$. They found that the peak forces during the gust were close to semi-empirical quasi-steady predictions for attached flow, but the transient forces after the gust peak were not. In a subsequent, complementary study [8], the same authors measured the force on flat-plates performing plunge maneuvers exceeding significantly the limits of small-perturbation approximation. The experiments covered a wider range of Reynolds numbers ($Re \approx 1000 - 37000$) and gust ratios ($G = V/U_\infty = 0.2 - 22$, were $V$ is the maximum plunge velocity). They found that the quasi-steady predictions were reasonably accurate for cases with low to moderate unsteadiness, similar to the results obtained for localized gusts [6].

The similitude between transverse localized gusts and plunge/pitch maneuvers was also explored by Leung et al. [9], using 2D simulations. They considered a $Re = 1000$ and gust ratios $G = V/U_\infty = 0.27$ and 0.57, for different durations of the gust. The plunge and plunge-pitching motions considered in this study were selected to match the histories of effective angle of attack of the airfoil as it crossed the localized transverse gust. Their results showed that the force coefficients obtained in the plunge maneuvers agree well with the localized gusts when the gust is sufficiently wide

(i.e., $k = \pi c/\lambda < 0.5$, where $\lambda$ is the width of the one-minus-cosine transverse gust). For more localized gusts, the differences in the force coefficients were ascribed to 1) the nonlinear angle of attack distribution over the airfoil in the localized gusts, and 2) the interactions between the localized gust vorticity and the wake of the airfoil, which prevents the roll-up of the trailing edge vorticity observed in the plunging/pitching maneuvers.

In the present work we consider Direct Numerical Simulations (DNS) of large-amplitude plunging maneuvers, similar to the experiments of Perrotta and Jones[8], but at somewhat higher Reynolds number and velocity ratios than in Leung et al [9]. In particular, we intend to characterize the influence of the Reynolds number on the aerodynamic forces by performing simulations at $Re = 1000$ and 5000. Note that, even if the flow configuration is geometrically two-dimensional, the flow around a moving airfoil is truly two-dimensional only at low $Re$. For example, in the plunging simulations of Visbal [7], the flow was 2D at $Re = 1000$ and 3D at $Re = 5000$ (see Fig. 22 in the cited article). Thus, for Reynolds number larger than $Re \approx 1000$, and depending on the the airfoil motion, the flow starts to develop 3D features[12–15]. In such cases, a 2D-DNS probably does not provide an accurate representation of the flow since the vortex stretching term, which plays an important role in the 3D dynamics of the flow, vanishes identically in 2D. Recent literature include works using 2D DNS simulations at $Re$ beyond $Re = 1000$; for instance Ref. [16] reports the use of a 2D DNS to study the performance augmentation of in-line tandem foils at $Re = 7000$. Whether this affects the estimation of the aerodynamic forces is an open question that we explore in this work. To this aim we present results of 2D-DNS and 3D-DNS of the same plunging maneuver at $Re = 5000$.

## II. Problem description

The problem setup consists of a wing of infinite aspect ratio subject to a plunging maneuver in the presence of a uniform free stream of velocity $U_\infty$. The wing section is a NACA 0012 airfoil of chord $c$. The angle of attack with respect to the free stream is $\alpha = 5^\circ$ for all cases considered. The plunge maneuver is modeled after a sine-squared transverse gust profile, as in Perrotta and Jones [8]. The vertical displacement of the airfoil is denoted $h(t)$, so that the plunge velocity is given by

$$\dot{h} = -V \sin^2\left(\pi \frac{t - t_0}{T}\right) \quad \text{if} \quad t_0 < t < t_0 + T, \tag{1a}$$

$$\dot{h} = 0 \qquad\qquad \text{otherwise}, \tag{1b}$$

where $V$ is the maximum vertical velocity of the airfoil and $t_0$ and $T$ are the starting time and duration of the maneuver, respectively. We keep constant the duration of the maneuver $TU_\infty/c = 2$ and set $t_0 = 0$. We consider three values of the velocity ratio $G = V/U_\infty = 0.5$, 1 and 2. Note also that the final vertical position of the airfoil for the current duration of the maneuver is $h(T)/c = -G$. Two values for the Reynolds number of the flow, based on $U_\infty$ and $c$, are considered, $Re = 1000$ and 5000. We perform 2D simulations for the reported values of $G$ and $Re$. Additionally, for $G = 1$ and 2 at

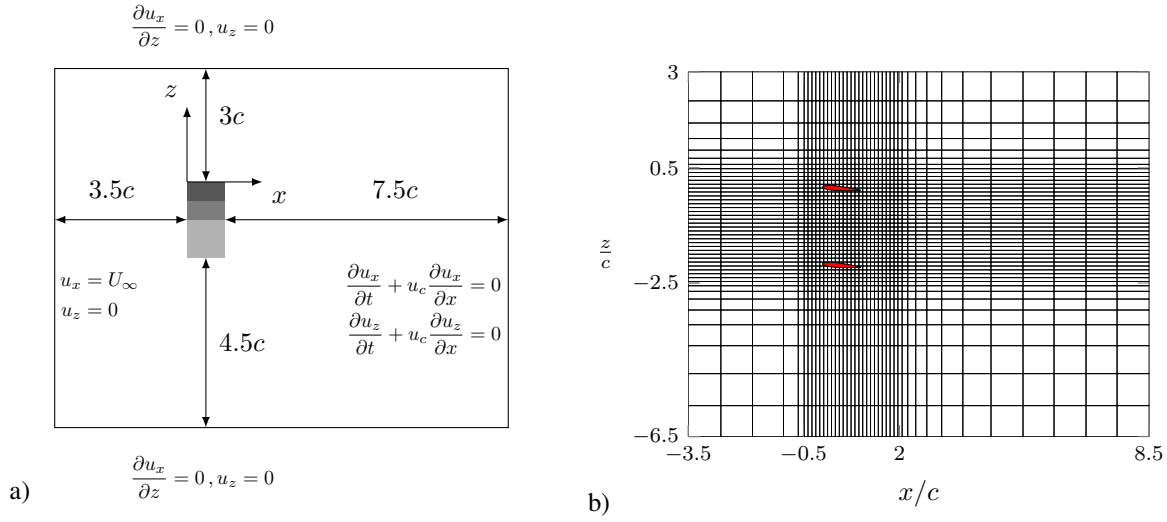


**Fig. 1 a) Sketch of the computational domain and b) visualization of the grid showing 1 every 32 grid lines. Both panels correspond to $Re = 5000$.**

$Re = 5000$, we also perform 3D simulations, as summarized in Table 1.

The simulations presented here have been performed with TUCAN, an extensively validated in-house code that solves the incompressible Navier–Stokes equations on a non-uniform Cartesian staggered grid [17, 18]. The spatial discretization is made with the second order finite differences scheme described in Vasilyev [19] to ensure mass and momentum conservation. Time marching is performed by means of a semi-implicit three-stage, low-storage Runge Kutta scheme [20, 21] together with the fractional step method described in Brown [22] to fulfill the continuity constraint. The presence of the wing is modeled with the direct forcing immersed boundary method proposed by Uhlmann [23]. TUCAN has been successfully employed in flapping wing studies of infinite [14, 24, 25] and finite [26–29] aspect ratio wings.

We have selected the grid resolution after performing a grid refinement study. For all cases we employ a uniform grid in the vicinity of the airfoil ($-0.5 < x/c < 2$, $-2.5 < z/c < 0.5$), where the leading edge of the airfoil is at $x/c = 0$ and the displacement of the airfoil ($h(t)$) is measured with respect to $z = 0$. For the simulations with $Re = 1000$, we use 160 points per chord ($c/\Delta x = 160$) near the airfoil, with a stretching factor far from the airfoil of 1.01. The computational domain size is $25c$ and $20c$ in the streamwise, $x$, and vertical, $z$, directions, respectively. This results in a grid with 982 and 1042 points in the streamwise and vertical directions, respectively. For the simulations with $Re = 5000$, we use $c/\Delta x = 320$ near the airfoil and a stretching factor far from the airfoil of 1.01 in every direction except upstream, where a stretching factor of 1.03 is used. The computational domain size is $12c$ and $9.5c$ in $x$ and $z$, respectively. This results in a grid with 1335 and 1459 points in the streamwise and vertical directions, respectively. For the 3D simulations, the spanwise size of the computational domain is $L_y = c/4$ with a uniform mesh, so that 80 points

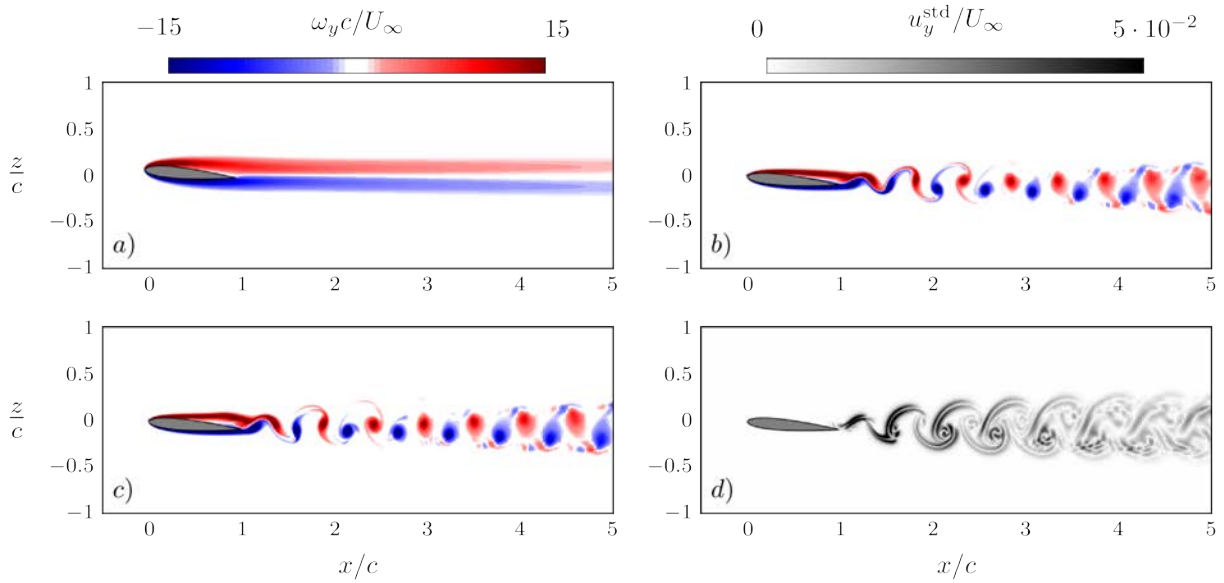


**Fig. 2 Initial conditions for the plunge maneuvers. (a-c) Red-blue for $\omega_y$. (d) Black-white for $u_y^{std}$. (a) 2D1, (b) 2D5, (c,d) 3D5.**

are used along this direction.

Dirichlet boundary conditions are imposed at the inlet with a uniform free-stream velocity. At the outlet a convective boundary condition is employed. Free slip boundary conditions are imposed at the top and bottom boundaries. Finally, for the 3D simulations periodic boundary conditions are imposed along the spanwise direction in order to model a wing with infinite span. A sketch of the computational domain, boundary conditions and the grid of the cases with $Re = 5000$ can be seen in Figure 1. The gray areas in Figure 1a correspond to the area swept by the airfoil for the three values of $G$ considered here. The red airfoils in Figure 1b show the initial and final positions of case $G = 2$.

In the following, we denote the three velocity components as $u_x$, $u_y$ and $u_z$, and the spanwise vorticity $\omega_y = \frac{\partial u_x}{\partial z} - \frac{\partial u_z}{\partial x}$. For the 3D simulations, we define flow quantities averaged along the span. For any quantity $\phi$, $\overline{\phi}$ denotes the corresponding spanwise-average defined as

$$\overline{\phi}(x, z, t) = \frac{1}{L_y} \int_0^{L_y} \phi(x, y, z, t)\, \mathrm{d}y, \tag{2}$$

and $\phi^{\mathrm{std}}$ denotes the standard deviation defined as

$$\phi^{\mathrm{std}}(x, z, t) = \sqrt{\frac{1}{L_y} \int_0^{L_y} \left(\phi(x, y, z, t) - \overline{\phi}(x, z, t)\right)^2 \mathrm{d}y}. \tag{3}$$

The simulations are run initially for several non-dimensional time units, while the airfoil wake develops, see Figure 2. Then, time is set to zero and the plunge maneuver begins. For the 3D simulations, 3D effects are developed during this initial transient, but remain localized to the wake of the airfoil. The flow over the rest of the airfoil remains attached

**Table 1 Parameters of the simulations. Dim indicates if the simulation is 2D or 3D.**

| Case | 2D1-A | 2D1-B | 2D1-C | 2D5-A | 2D5-B | 2D5-C | 3D5-B | 3D5-C |
|---|---|---|---|---|---|---|---|---|
| Re | 1000 | 1000 | 1000 | 5000 | 5000 | 5000 | 5000 | 5000 |
| G | 0.5 | 1.0 | 2.0 | 0.5 | 1.0 | 2.0 | 1.0 | 2.0 |
| dim | 2 | 2 | 2 | 2 | 2 | 2 | 3 | 3 |

and two-dimensional, as it can be observed in Figure 2d.

## III. Results

We start analyzing the force coefficients for different values of $G$. First, let us define the drag and lift coefficients as

$$c_d = \frac{F_x}{\frac{1}{2}\rho U_\infty^2 c}, \tag{4a}$$

$$c_l = \frac{F_z}{\frac{1}{2}\rho U_\infty^2 c}, \tag{4b}$$

where $F_x$ and $F_z$ are the aerodynamic forces per unit span in the streamwise and vertical directions, respectively. In the 3D cases $F_x$ and $F_z$ are computed dividing the aerodynamic force by the span $L_y$, whereas in the 2D simulations $F_x$ and $F_z$ are directly the forces per unit span. Figure 3 shows the drag and lift time evolution for the cases with $Re = 1000$, together with the vertical position and velocity of the airfoils. Overall, the time evolution of the force coefficients is qualitatively similar for all cases except for a somewhat higher complexity of the $c_d$ profile when $G = 2$, with additional maxima appearing at $tU_\infty/c \approx 1$ and 4.5. For all cases the time evolution can be split into four parts. The first part ($t < 0$) corresponds to the initial phase before the maneuver is initiated. This phase is characterized by constant values of $c_d = 0.13$ and $c_l = 0.24$. The second part corresponds to the acceleration of the airfoil during the interval $0 < t < T/2$; recall that $T = 2c/U_\infty$ for all maneuvers. In this phase the lift coefficient shows a continuous growth until slightly before $t = T/2$, where the lift starts to decrease. The time at which $c_l = c_l^{\text{peak}}$ is approximately the same for the three cases shown in the figure. Concerning the drag coefficient, all three cases present positive values of $c_d$ during this phase. The third part corresponds to the deceleration of the airfoil during the interval $T/2 < t < T$, where $c_l$ decreases and $c_d$ is characterized by values lower than the static value, reaching negative values (i.e. thrust) for the case $G = 2$. After $t \approx 3T/4$, both the lift and drag coefficients reach local minima and then increase until the end of the maneuver ($t = T$). The final phase corresponds to the recovery of the flow after the maneuver has finished ($t > T$); in this phase the lift coefficient decreases slowly towards the static values. Note that higher values of $G$ seems to result in longer decay times. For example, at $tU_\infty/c = 5$ the static value for cases $G = 0.5$ and 1 has been recovered, but not for the case with $G = 2$. During the recovery, the drag coefficient does not decrease immediately after the end of the maneuver. Instead, it keeps growing for a while until eventually the decay begins. For cases with $G = 0.5$ and 1, once $c_d$ starts decaying, the static

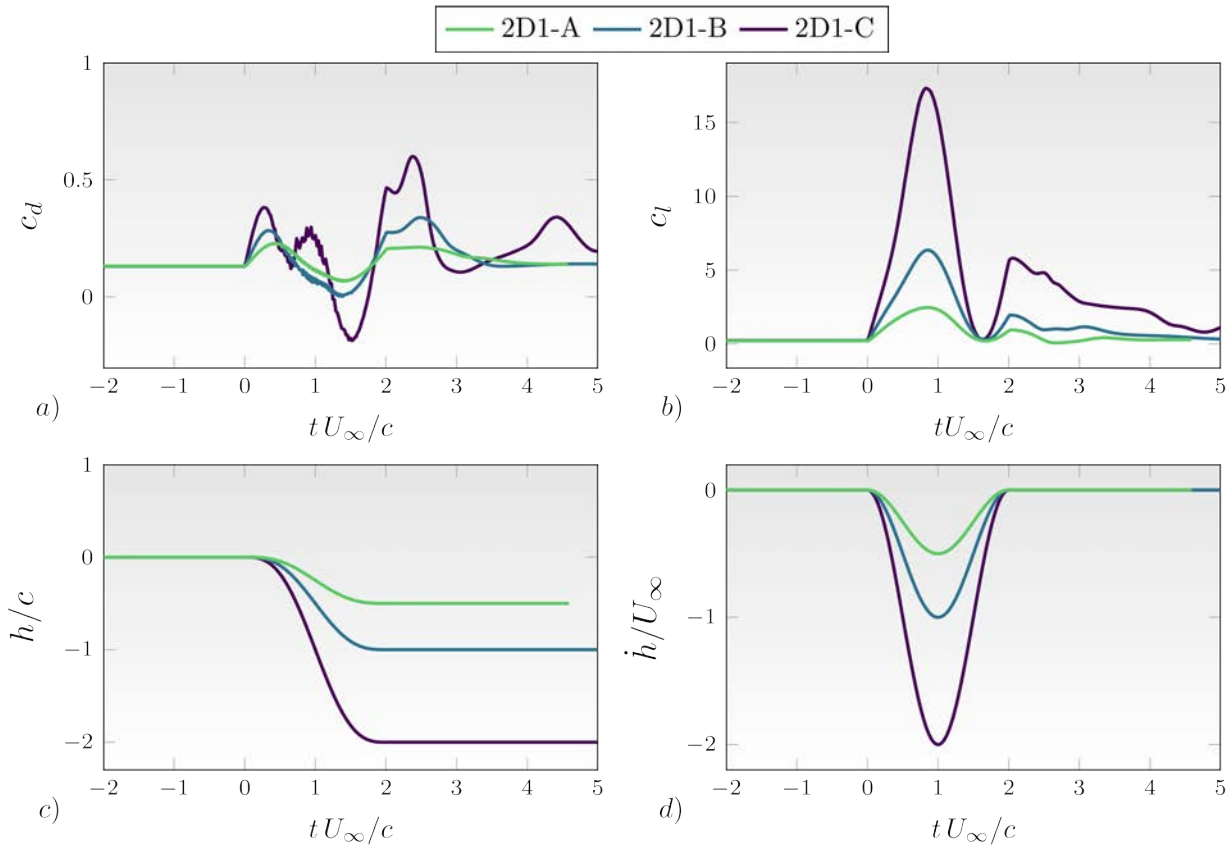


**Fig. 3 Time history of a) $c_d$, b) $c_l$, c) $h/c$ and d) $\dot{h}/U_\infty$ of maneuvers at $Re$ = 1000.**

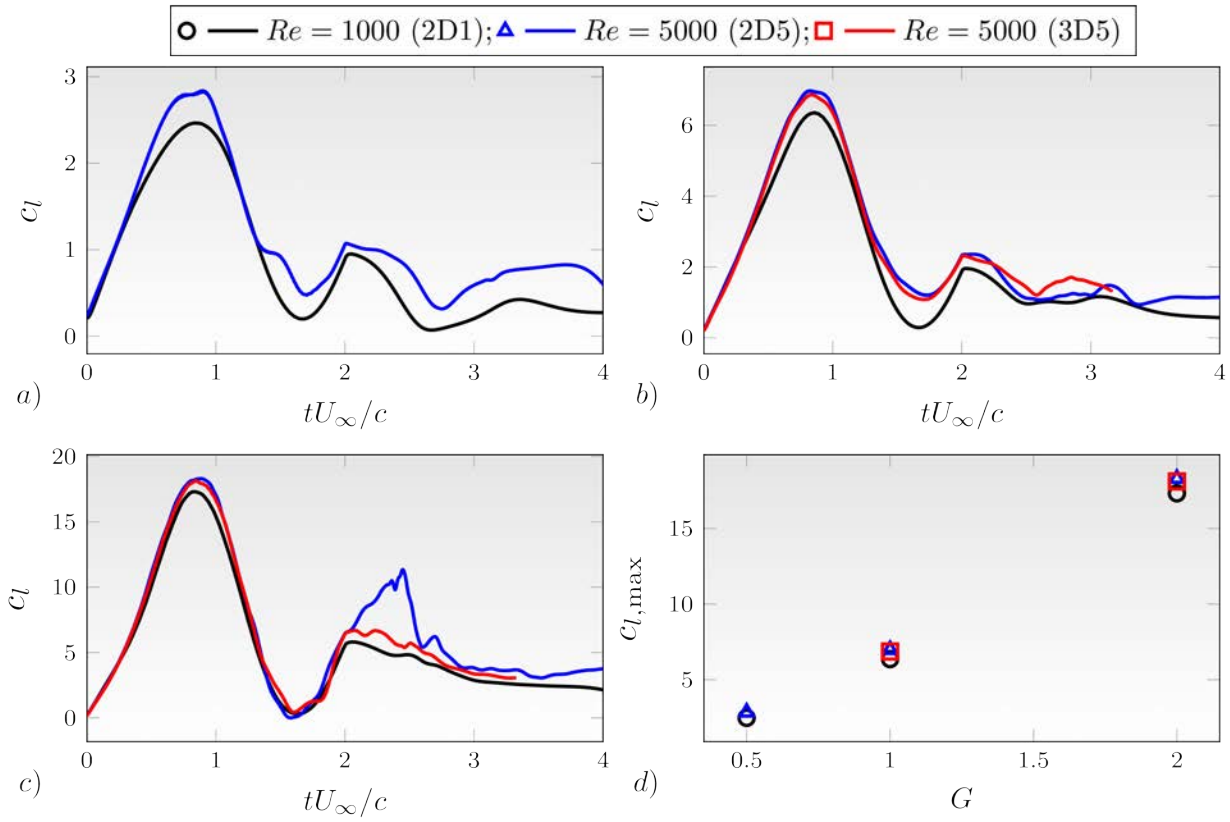


**Fig. 4 Time evolution of $c_l$ for all the cases. a) $G = 0.5$, b) $G = 1$ and c) $G = 2$, d) $c_l^{\text{peak}}$ as a function of $G$.**

values are eventually recovered. For case $G = 2$, the decay seems to occur in the form of damped oscillations, with a visible peak at $tU_\infty/c \approx 4.5$ which has an intensity twice weaker than that of the peak at $tU_\infty/c \approx 2.5$.

Figure 4 shows the lift coefficient for all cases of Table 1. Cases with $G = 0.5$ are shown in panel a), $G = 1$ in panel b) and $G = 2$ in panel c). Finally, panel d) displays $c_l^{\text{peak}}$ as a function of $G$, showing a linear dependence of $c_l^{\text{peak}}$ with $G$ for the cases considered here. For $G = 0.5$ and $G = 1$, the time evolution of $c_l$ is qualitatively the same independent of the Reynolds number. Note that somewhat higher values of $c_l$ are obtained for the cases with $Re = 5000$ compared to the cases with $Re = 1000$. Moreover, the effect of the three-dimensionality on case $G = 1$ is also very small. The effect of the Reynolds number on $c_l$ is also small for case $G = 2$ during the maneuver (i.e., $t < T$). However, clear discrepancies are observed during the recovery phase, where case 2D5-C presents a pronounced peak at $t \approx 2.5c/U_\infty$ which is not present in cases 2D1-C and 3D5-C. Since the flow at $Re = 5000$ is expected to be affected by 3D effects, as discussed in the introduction, this pronounced peak for case 2D5-C is likely to be unphysical.

In order to explore the similarities and differences between the three simulations with $G = 2$, we proceed to analyze the corresponding flow fields. Figure 5 shows instantaneous contours of the spanwise vorticity $\omega_y$ for the 2D simulations, whereas for the 3D simulation contours of $\overline{\omega}_y$ are shown together with shaded-contours of $u_y^{\text{std}}$. The shaded-contours of

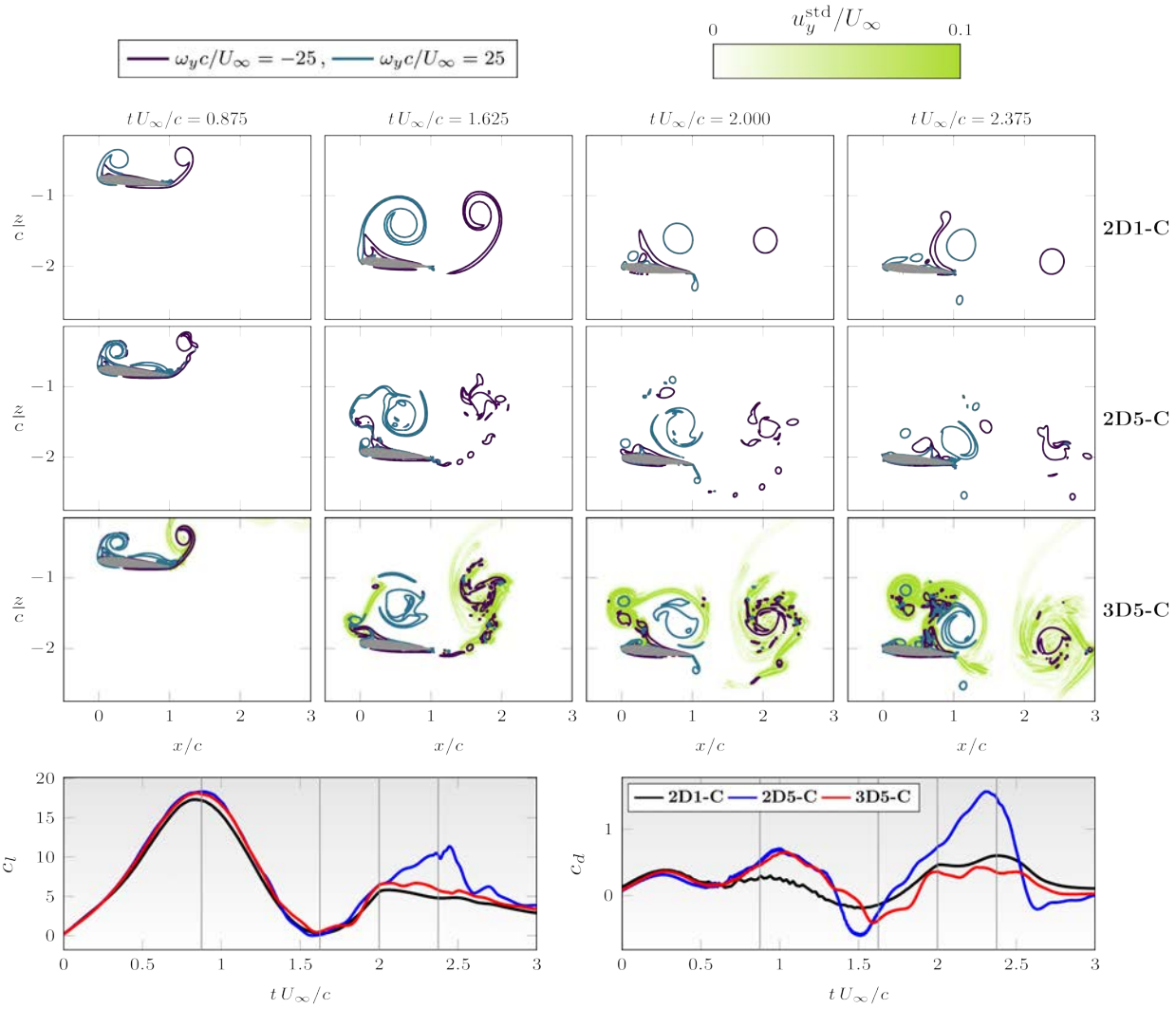


**Fig. 5 Contours of $\omega_y$ and $u_y^{\mathrm{std}}$ for the three configurations (2D1-C, 2D5-C and 3D5-C) for $G = 2$. The bottom row shows $c_l$ and $c_d$ as a function of time.**

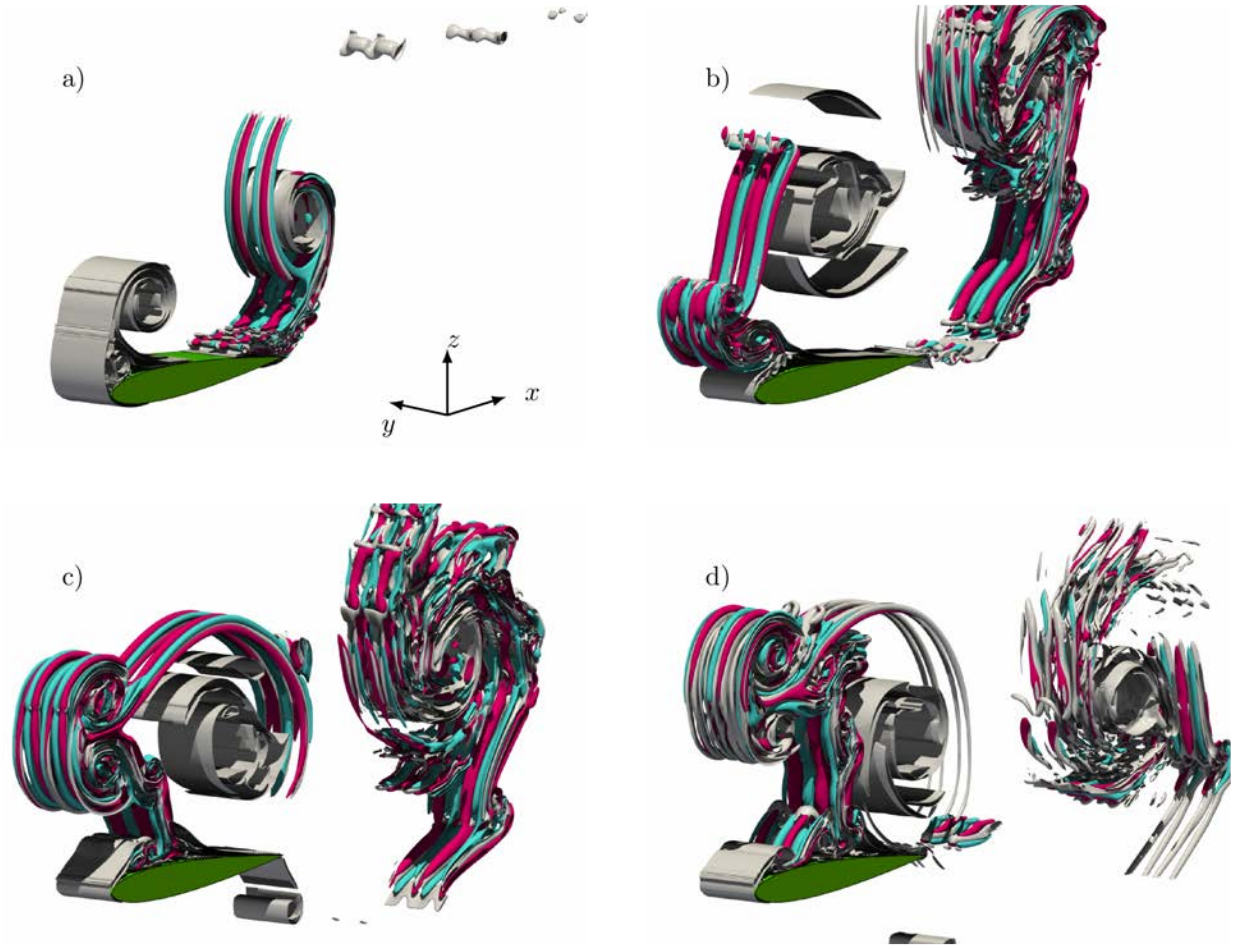


**Fig. 6 Flow visualization of the case 3D5-C. The time instants are a)** $t/T = 0.875$**, b)** $t/T = 1.625$ **and c)** $t/T = 2.0$ **and d)** $t/T = 2.375$**.**

the standard deviation of the spanwise velocity fluctuations are used to identify those regions where 3D effects are present. In addition, Figure 6 shows the corresponding 3D visualizations using iso-surfaces of the second invariant of the velocity gradient tensor, $Q$, and iso-surfaces of spanwise velocity fluctuations. For the visualizations, four representative time instants have been selected: two during the maneuver, corresponding roughly to maximum $c_l$ ($t = 0.875c/U_\infty$) and minimum $c_l$ ($t = 1.625c/U_\infty$), the third one at the end of the maneuver ($t = 2c/U_\infty$), and the last one during the recovery phase corresponding roughly to the maximum $c_l$ difference between the cases ($t = 2.375c/U_\infty$). The following comments are based on these visualizations and on corresponding animations covering the whole integration interval.

First, during the acceleration phase, a positive vorticity Leading Edge Vortex (LEV) and a negative vorticity Trailing Edge Vortex (TEV) are formed on the upper part of the airfoil. These vortices are visible at $t = 0.875c/U_\infty$ relatively close to the airfoil (first column of Figure 5). In such a configuration, it is well known that the contribution of the LEV to $c_l$ is very significant [30]. For the three simulations, the flow topology is very similar, and correspondingly

the aerodynamic forces at this instant are similar. Note that for the 3D simulation, 3D effects are confined to a region surrounding the TEV, while the LEV remains two-dimensional. This is clearly visible in Figure 6a, which shows iso-surfaces of $Q$ (in gray) together with iso-surfaces of spanwise velocity, $u_y/U_\infty = \pm 0.1$ (in blue and pink). Recall that, the initial condition before the maneuver corresponds to uniform incoming flow over the stationary airfoil. In this initial condition, 3D effects are found near the trailing edge only. Then, it is not surprising that, during the acceleration phase of the maneuver, 3D effects are only found near the TEV and do not have time to be propagated upstream.

During the deceleration phase, LEV and TEV keep on growing in size and eventually detach from the airfoil. A dipole is formed below the LEV that remains near the leading edge of the airfoil. In the 3D simulation, during this phase the 3D effects are intensified around the trailing edge and propagate upstream, to eventually reach the leading edge. By the time shown in the second column of Figure 5, $t = 1.625c/U_\infty$, the LEV has clearly detached from the airfoil in all three simulations. The main flow topology is still rather similar, although clearly smoother for the case with $Re = 1000$ (2D1-C). The qualitative differences between the three simulations at this instant are mostly limited to the dipole below the LEV. In case 2D1-C the dipole remains attached to the airfoil. In case 2D5-C, the rolling of the LEV has split the dipole apart, lifting up and engulfing the vortex with negative vorticity. In case 3D5-C, the interaction between the dipole and the LEV is clearly influenced by 3D effects as evidenced by the shaded contour of spanwise velocity fluctuations connecting these two structures, see also Figure 6b. The result of this interaction is a different flow topology than in case 2D5-C, with the dipole remaining closer to the airfoil. Actually, the flow topology in 3D5-C is more similar to the topology found in case 2D1-C than the topology found in 2D5-C. In any case, these differences are still subtle, not having a significant impact on the force coefficients yet.

During the rest of the maneuver, the overall evolution of the LEV and the TEV remains similar in the three simulations. The TEV is convected downstream so that, most likely, its influence on the force coefficients becomes negligible. On the other hand, the LEV approaches the rear part of the airfoil as the latter decelerates and stops. As a consequence, the subtle differences in the flow topology observed in previous instants are amplified by the motion of the LEV. In case 2D5-C, the approaching LEV displaces the vortex previously lifted from the leading edge, resulting in a relatively clean leading edge at $tU_\infty/c = 2.375$. In case 2D1-C, the LEV stretches the negative voticity of the leading edge dipole, generating an elongated shear layer and leaving an emerging LEV at $t = U_\infty/c = 2.375$. In case 3D5-C, the dipole observed at $tU_\infty/c = 1.625$ near the leadging edge detaches from the airfoil, leaving an stretched shear layer of negative vorticity behind. The latter is lifted up by the LEV in a similar way as in case 2D1-C, resulting also in an elongated layer, which is more disorganized and subjected by 3D effects.

In summary, at $t = 2.375c/U_\infty$, the flow topology around the airfoil is more similar in cases 3D5-C and 2D1-C than in case 2D5-C, due to the diferences in the interactions between the approaching LEV and the small dipole at the leading edge. It seems reasonably to assume that these interactions explain the similitudes and differences previously discussed in the evolution of the force coefficients of these 3 cases during the recovery phase. Additional support to

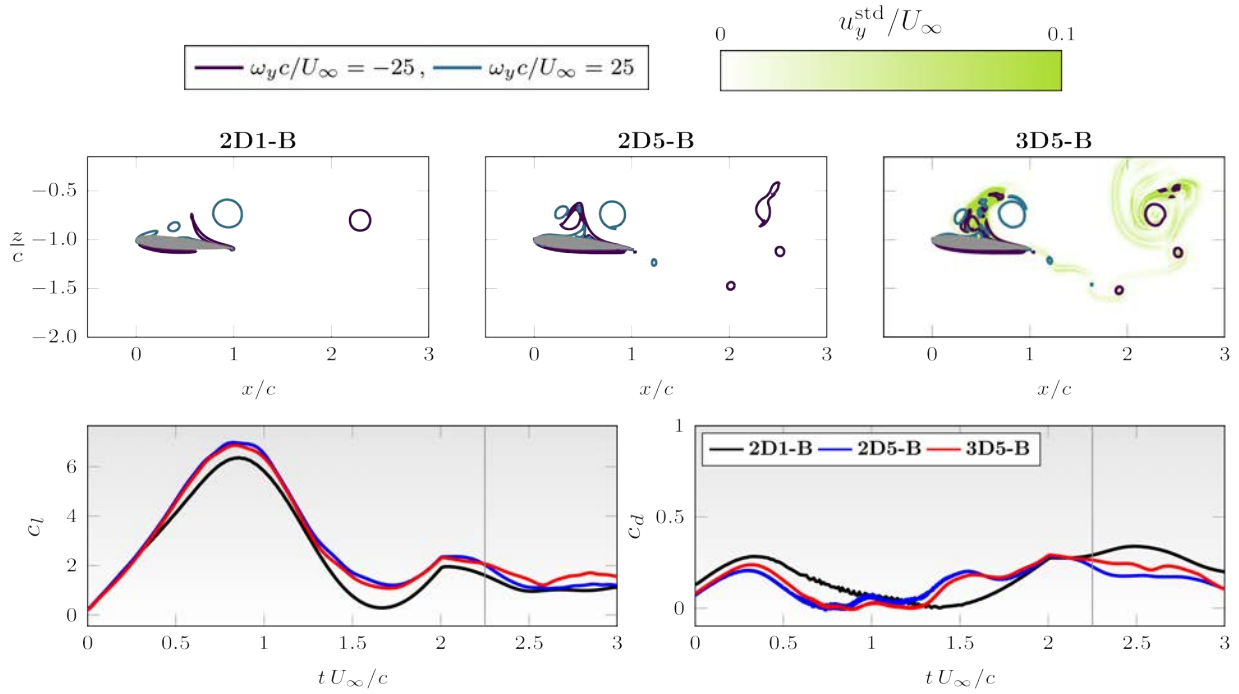


**Fig. 7 Contours of $\omega_y$ and $u_y^{\mathrm{std}}$ for the three configurations (2D1-B, 2D5-B and 3D5-B) for $G = 1$ at $t/T = 2.25$. The bottom row show $c_l$ and $c_d$ as a function of time.**

this observation can be obtained by analyzing the plunge maneuver with $G = 1$, which is less violent than the plunge maneuver with $G = 2$. It was already discussed in Figure 4b, that the time evolution of the lift coefficient for all three simulations with $G = 1$ is qualitatively similar. Figure 7 shows a flow visualization of these three cases, equivalent to the flow visualization for case $G = 2$ shown in Figure 5. In Figure 7 only a time instant in the recovery phase is shown. The flow topology observed for the three cases is rather similar. A smaller LEV (compared to the $G = 2$ simulations) is found in the rear part, flanked at its left by a lifted-up region of negative vorticity. Accordingly the force coefficients do not present significant differences between the three cases.

Finally, to close the article, we compare the present DNS results to the experimental results of Perrotta and Jones [8] (PJ18 in the following). Two of the cases of their database correspond to the same plunge maneuvers presented here for $G = 1$ and $G = 2$. Figure 8 shows $\Delta c_l = c_l - c_{l\mathrm{static}}$ as a function of time for both PJ18 and the present DNS results, where $c_{l\mathrm{static}}$ is the static value of the lift coefficient at the angle of attack considered in each case. Note the different scales for the lift coefficient in panel *a*) ($G = 1$) and *b*) ($G = 2$). The overall agreement is only qualitative, with both curves presenting similar trends. It is encouraging that the main $\Delta c_l$ peak in the accelerating phase ($0 < tU_\infty/c < 1$) is well predicted by the simulations for both $G = 1$ and 2. However, large discrepancies are observed in the decelerating phase ($1 < tU_\infty/c < 2$) where the minimum $\Delta c_l$ is very negative in the experiments while it remains close to zero in the DNS. Following this minimum, the $\Delta c_l$ grows reaching a second peak. For the case $G = 2$ the amplitude of this growth

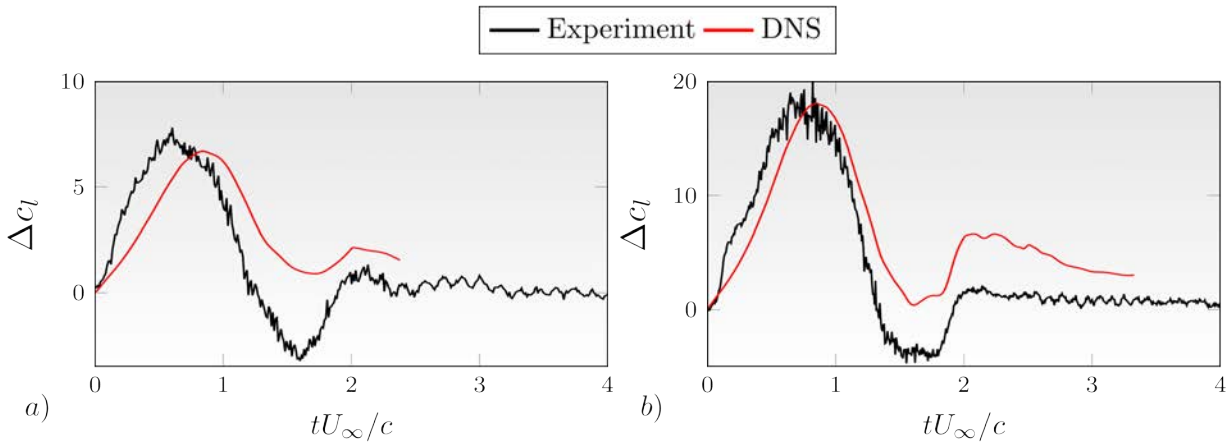


**Fig. 8 $\Delta c_l$ as a function of time. Black line, experiments [8]. Red line, present DNS. a) $G = 1$ and b) $G = 2$.**

is similar in experiments and simulations. Once the maneuver is finished ($tU_\infty/c > 2$), the relaxation to the static value takes much longer in the DNS than in the experiments. This is particularly clear for the case $G = 2$ where the simulation was integrated for a longer time interval.

The fact that, overall, only qualitative agreement is observed between our DNS and PJ18 can be ascribed to a few significant differences between experimental and computational setups. First, PJ18 employed a flat plate at $\alpha = 0°$ while the DNS was perfomed using a NACA0012 at $\alpha = 5°$. The Reynolds number of the incoming flow is also somewhat different, $Re \approx 20000$ in PJ18 and $Re = 5000$ in the DNS. Finite wing effects might also influence $\Delta c_l$; while in the experiments a wing of aspect ratio 4 was studied, in the DNS an infinite aspect ratio wing is modelled by considering periodic boundary conditions along the spanwise direction in a domain $L_y = c/4$. The domain size in the DNS could also have an impact on the results. There are also differences in the incoming flow. In the DNS a uniform flow is imposed at the inflow while in the experiments perturbations are unavoidable. It is therefore likely that all these effects influence the lift coefficient leading to the discrepancies observed between experiments and simulations. For example, the longer relaxation time in the DNS might be the result of a combined effect between airfoil shape and angle of attack. Note for example, that, once the maneuver is finished, a flat plate at $\alpha = 0°$ represents a smaller perturbation to the flow than a NACA0012 airfoil at $\alpha = 5°$. How each of the mentioned effects influence the lift coefficient is worth investigating. This hopefully will be done in future studies.

## IV. Conclusions

We have presented a series of 2D and 3D direct numerical simulations of plunging maneuvers at Reynolds number $Re = 1000$ and 5000 and with velocity ratios $G = 0.5$, 1 and 2. The calculations were performed by solving the Navier–Stokes equations using an immersed boundary method, prescribing the motion of the wing. We have analyzed the time evolution of the force coefficients during tha maneuvers and during the recovery to the static values. We have

also analyzed the flow structures (leading edge vortex, trailing edge vortex, a small dipole below the LEV) appearing in the neighbourhood of the airfoil and we have also discussed their interactions.

We have found that the influence of the Reynolds number on the time evolution of the force coefficients is small, obtaining somewhat larger values for $Re = 5000$. The time evolution of the force coefficients was also found to be qualitatively similar when varying the velocity ratio of the maneuver. The lift coefficient presents a pronounced peak towards the end of the acceleration phase of the maneuver, whose amplitude increases linearly with $G$, at least for the cases considered here. During this phase an intense LEV is formed on the upper part of the airfoil that remains attached to the airfoil. During the deceleration phase, $c_l$ decreases as the LEV detaches, eventually reaching a local minimum. Then, it grows again until the airfoil is completely stopped. This growth in the $c_l$ occurs at the same time as the LEV approaches again the airfoil, along its rear part. In the final phase, the transient decay towards the static values is found to be longer for increasing $G$, which is probably related to the fact that the intensity of the LEV is stronger for increasing $G$.

By performing 2D and 3D simulations of the maneuvers with $G = 1$ and 2 at $Re = 5000$, we have explored the predictive ability of the (unphysical) 2D simulations. It has been found that for $G = 1$ and $G = 2$, the main peak in the lift time evolution was correctly predicted by the 2D simulations. This was attributed to the fact that, during the maneuver, the intense LEV is little affected by 3D effects, and as a consequence, the $c_l$ during the maneuver is governed by 2D effects. However, significant differences were observed between the 2D and 3D calculations for the case with $G = 2$, during the recovery phase after the maneuver. It was observed that the interactions between the LEV and the small dipole formed below it present subtle differences (in 2D and 3D simulations) towards the end of the maneuver. In the subsequent evolution, these differences are amplified leading to an unphysical peak in the $c_l$ prediction of the 2D simulation. Thus, not surprisingly, the predictions of force coefficients of 2D simulations can not be trusted at moderate Reynolds numbers.

Finally, we have compared the results of the 3D calculations with the experimental data of Perrotta and Jones [8], obtaining a good qualitative agreement. However, some quantitative discrepancies were observed that may be attributed to differences in computational and experimental setups. Some of the factors that could be causing these differences are finite aspect ratio wing (experiment) vs infinite aspect ratio wing (simulations), and the combination of airfoil shape and angle of attack. From the point of view of the aspect ratio of the wing, the current DNS study is somewhat limited by the size of the computational domain in spanwise direction. A small domain size might constrain the non-linear evolution of the LEV, possibly influencing the force coefficients. This should be investigated in further studies.

## Acknowledgments

This work was supported by grant `DPI2016-76151-C2-2-R` (AEI/FEDER, UE). The computations were partially performed at the supercomputer Picasso from the *Red Española de Supercomputación* in activity `FI-2018-2-0051`. We thank Dr. A. Jones and Dr. G. Perrotta for providing their experimental data.

## References


[1] Hoblit, F. M., *Gust loads on aircraft: concepts and applications*, AIAA, 1988.

[2] Bisplinghoff, R. L., Ashley, H., and Halfman, R. L., *Aeroelasticity*, Addisin-Wesley, 1957.

[3] Mueller, T. J., *Fixed and Flapping Wing Aerodynamics for Micro Air Vehicle Applications*, AIAA, 2001. doi:10.2514/4.866654.

[4] Granlund, K., Monnier, B., Ol, M., and Williams, D., "Airfoil longitudinal gust response in separated vs. attached flows," *Phys. Fluids*, Vol. 26, No. 2, 2014, p. 027103. doi:10.1063/1.4864338.

[5] Strangfeld, C., Müller-Vahl, H., Nayeri, C. N., Paschereit, C. O., and Greenblatt, D., "Airfoil in a high amplitude oscillating stream," *J. Fluid Mech.*, Vol. 793, 2016, pp. 79–108. doi:10.1017/jfm.2016.126.

[6] Perrotta, G., and Jones, A. R., "Unsteady forcing on a flat-plate wing in large transverse gusts," *Exp. Fluids*, Vol. 58, No. 8, 2017, p. 101. doi:10.1007/s00348-017-2385-z.

[7] Visbal, M. R., "Numerical investigation of deep dynamic stall of a plunging airfoil," *AIAA J.*, Vol. 49, No. 10, 2011, pp. 2152–2170. doi:10.2514/1.J050892.

[8] Perrotta, G., and Jones, A. R., "Quasi-steady approximation of forces on flat plate due to large-amplitude plunging maneuvers," *AIAA J.*, Vol. 56, No. 11, 2018, pp. 4232–4242. doi:10.2514/1.J057194.

[9] Leung, J., Wong, J., Weymouth, G., and Rival, D., "Modeling transverse gusts using pitching, plunging and surging airfoil motions," *AIAA J.*, Vol. 56, No. 8, 2018, pp. 3271–3278. doi:10.2514/1.J056961.

[10] Peng, D., and Gregory, J. W., "Vortex dynamics during blade-vortex interactions," *Phys. Fluids*, Vol. 27, No. 5, 2015, p. 053104. doi:10.1063/1.4921449.

[11] Barnes, C. J., and Visbal, M. R., "Counterclockwise vortical-gust/airfoil interactions at a transitional Reynolds number," *AIAA J.*, 2018, pp. 2540–2552. doi:10.2514/1.J056711.

[12] Deng, J., and Caulfield, C. P., "Three-dimensional transition after wake deflection behind a flapping foil," *Phys. Rev. E*, Vol. 91, No. 4, 2015, p. 043017. doi:10.1103/PhysRevE.91.043017.

[13] Deng, J., Sun, L., and Shao, X., "Dynamical features of the wake behind a pitching foil," *Phys. Rev. E*, Vol. 92, No. 6, 2015, p. 063013. doi:10.1103/PhysRevE.92.063013.

[14] Moriche, M., Flores, O., and García-Villalba, M., "Three-dimensional instabilities in the wake of a flapping wing at low Reynolds number," *Int. J. Heat and Fluid Flow*, Vol. 62, 2016, pp. 44–55. doi:10.1016/j.ijheatfluidflow.2016.06.015.

[15] Sun, L., Deng, J., and Shao, X., "Three-dimensional instabilities for the flow around a heaving foil," *Phys. Rev. E*, Vol. 97, No. 1, 2018, p. 013110. doi:10.1103/PhysRevE.97.013110.

[16] Muscutt, L. E., Weymouth, G. D., and Ganapathisubramani, B., "Performance augmentation mechanism of in-line tandem flapping foils," *J. Fluid Mech.*, Vol. 827, 2017, pp. 484–505. doi:10.1017/jfm.2017.457.

[17] Moriche, M., "A numerical study on the aerodynamic forces and the wake stability of flapping flight at low Reynolds number," Ph.D. thesis, Universidad Carlos III de Madrid, 2017.

[18] Gonzalo, A., "Aerodynamic forces and vortex structures of flapping wings in forward flight," Ph.D. thesis, Universidad Carlos III de Madrid, 2018.

[19] Vasilyev, O. V., "High order finite difference schemes on non–uniform meshes with good conservation properties," *J. Comput. Phys.*, Vol. 157, No. 2, 2000, pp. 746–761. doi:10.1006/jcph.1999.6398.

[20] Spalart, P. R., Moser, R. D., and Rogers, M. M., "Spectral methods for the Navier–Stokes equations with one infinite and two periodic directions," *J. Comput. Phys.*, Vol. 96, No. 2, 1991, pp. 297–324. doi:10.1016/0021-9991(91)90238-G.

[21] Rai, M., and Moin, P., "Direct simulations of turbulent flow using finite–difference schemes," *J. Comput. Phys.*, Vol. 96, No. 1, 1991, pp. 15–53. doi:10.1016/0021-9991(91)90264-L.

[22] Brown, D. L., Cortez, R., and Minion, M. L., "Accurate projection methods for the incompressible Navier–Stokes equations," *J. Comput. Phys.*, Vol. 168, No. 2, 2001, pp. 464–499. doi:10.1006/jcph.2001.6715.

[23] Uhlmann, M., "An immersed boundary method with direct forcing for the simulation of particulate flows," *J. Comp. Phys.*, Vol. 209, No. 2, 2005, pp. 448–476. doi:10.1016/j.jcp.2005.03.017.

[24] Moriche, M., Flores, O., and García-Villalba, M., "On the aerodynamic forces on heaving and pitching airfoils at low Reynolds number," *J. Fluid Mech.*, Vol. 828, 2017, pp. 395–423. doi:10.1017/jfm.2017.508.

[25] Moriche, M., Raiola, M., Discetti, S., Ianiro, A., Flores, O., and García-Villalba, M., "Assessing aerodynamic force estimation with experiments and simulations of flapping-airfoil flows on the verge of three-dimensionality," *Proc. Inst. Mech. Eng. G J. Aerospace Eng.*, Vol. 234, No. 2, 2020, pp. 428–444. doi:10.1177/0954410019867570.

[26] Gonzalo, A., Arranz, G., Moriche, M., García-Villalba, M., and Flores, O., "From flapping to heaving: A numerical study of wings in forward flight," *J. Fluids Struct.*, Vol. 83, 2018, pp. 293–309. doi:10.1016/j.jfluidstructs.2018.09.006.

[27] Arranz, G., Moriche, M., Uhlmann, M., Flores, O., and García-Villalba, M., "Kinematics and dynamics of the auto-rotation of a model winged seed," *Bioinspir. Biomim.*, Vol. 13, 2018, p. 036011. doi:10.1088/1748-3190/aab144.

[28] Arranz, G., Gonzalo, A., Uhlmann, M., Flores, O., and García-Villalba, M., "A numerical study of the flow around a model winged seed in auto-rotation," *Flow Turbul. Combust.*, Vol. 101, No. 2, 2018, pp. 477–497. doi:10.1007/s10494-018-9945-z.

[29] Arranz, G., Flores, O., and García-Villalba, M., "Three-dimensional effects on the aerodynamic performance of flapping wings in tandem configuration," *J. Fluids Struct.*, Vol. 94, 2020, p. 102893. doi:10.1016/j.jfluidstructs.2020.102893.

[30] Eldredge, J. D., and Jones, A. R., "Leading-edge vortices: mechanics and modeling," *Annu. Rev. Fluid Mech.*, Vol. 51, 2019, pp. 75–104. doi:10.1146/annurev-fluid-010518-040334.

## A. Grid refinement study

In order to select the resolution used for the cases at higher Reynolds number ($Re = 5000$) we have performed several simulations of the most restrictive maneuver ($G = 2$) with various grids. We have varied the grid spacing in the vicinity of the airfoil $\Delta x$. The computational domain, the stretching factor and the refined area are the same as described in II for the cases with $Re = 5000$. The lower resolution used is $c/\Delta x = 164$, which is similar to the resolution used for cases with $Re = 1000$. From that value of $c/\Delta x$, the resolution is increased with a constant factor of 1.25 up to the highest value of $c/\Delta x = 400$. The time step for the case with $c/\Delta x = 400$ is $\Delta t U_\infty/c = 1/6400$ and for the rest of the cases, this value is modified accordingly to obtain the same CFL in every simulation. The boundary conditions and the initial condition are the same as described in II. This corresponds to inflow-outflow in the streamwise direction, free-slip in the vertical direction and the maneuver starts from a converged flow field in which the airfoil is static.

In order to select the grid resolution, we have analyzed the lift coefficient and the vorticty contours at $t\,U_\infty/c = 1$, when the plunge velocity $\dot{h}$ and the lift coefficient are maximum. Figures 9a and b show the evolution of the lift coefficient for the different values of $c/\Delta x$ evaluated. It can be seen that cases with $c/\Delta x \leq 164$ show an oscillatory behavior close to the peak and that there is no variation in the behavior of the lift force from the case with $c/\Delta x = 320$ to $c/\Delta x = 400$. Also, the differences in the flow field observed in figure 9c are not present in figure 9d, where only small differences can be appreciated. Therefore, we perform the simulations with $Re = 5000$ with a resolution of $c/\Delta x = 320$.

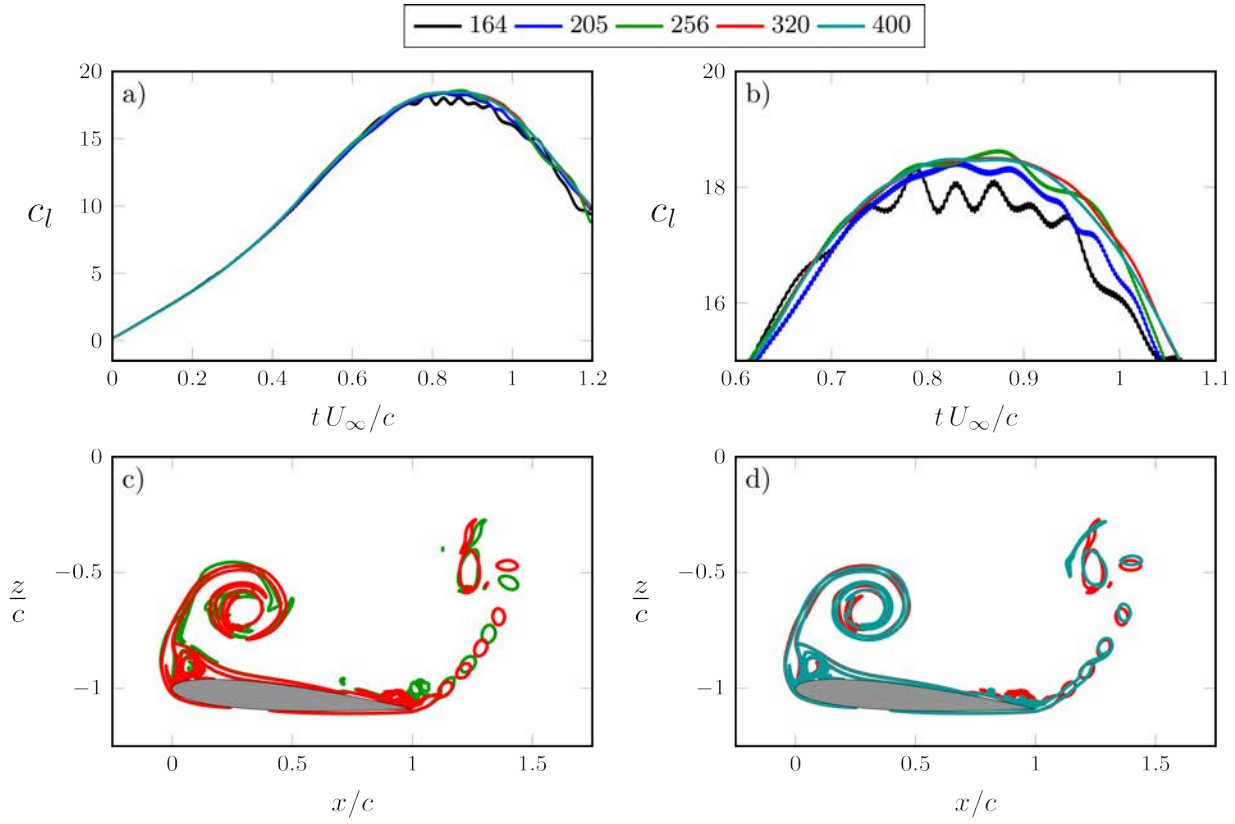


**Fig. 9 a) Time history of lift coefficient for a maneuver with $G = 2$, $w/c = 2$ at $Re = 5000$. Different curves correspond to different values of $c/\Delta x$ as indicated in the legend. b) A zoom of a) around the lift peak. c) and d) Vorticity contours at $tU_\infty/c = 1$, ($\omega_y c/U_\infty = \pm 50$). c) $c/\Delta x = 256, 320$ and d) $c/\Delta x = 320, 400$**